Redundancies in X-ray images due to the epipolar geometry for transmission imaging

André Aichert, Nicole Maass, Yu Deuerling-Zheng, Martin Berger, Michael Manhart, Joachim Hornegger, Andreas K. Maier and Arnd Doerfler

***Abstract*—In Computer Vision, the term epipolar geometry describes the intrinsic geometry between two pinhole cameras. While the same model applies to X-ray source and detector, the imaging process itself is very different from visible light. This paper illustrates the epipolar geometry for transmission imaging and makes the connection to Grangeat's theorem, establishing constraints on redundant projection data along corresponding epipolar lines. Using these redundancies, a geometric consistency metric is derived. Our metric could be applied to any pair of transmission images and could be used for pose refinement, calibration correction and rigid motion estimation in fluoroscopy and flat detector computed tomography (FD-CT) . In addition to the theoretical contribution, this paper investigates the properties and behavior of the metric for the purpose of re-calibration of an FD-CT short scan for narrow angular range.**

I. Introduction

In order to reconstruct a 3D image from a number of 2D X-ray projections, one requires accurate knowledge of the underlying projection geometry. The trajectory for CT reconstruction is either assumed fixed by construction or are calibrated before acquisition. Artifacts in the reconstruction may arise from inaccuracies of the calibration and unpredictable or non-reproducible scanner motion. This is also equivalent to rigid movement of the patient in medical scenarios.

Each image is associated with a projection matrix, which uses the same pinhole camera model as it is common in Computer Vision. The analogy opens up a field of established methods which are ready for application to transmission imaging problems [1], [2]. This paper studies the connection between the epipolar geometry of two projections and Grangeat's theorem [3] in order to exploit redundancies in the projection data for image-based optimization of the assumed projection geometry after an acquisition. Both the epipolar geometry and Grangeat's Theorem have previously been used for this purpose [4], [5], but their connection has not been established. In contrast to [6], [5], the work of Debbeler et al. [4] does not require reconstruction and uses a relatively simple and fast metric on 2D projections. We derive a new formulation of that metric based on epipolar geometry, which allows us to model the reliability in a certain direction given a specific trajectory. Finally, we will investigate accuracy, precision and robustness of the X-ray source and detector, specifically for subsets of a short scan trajectory of an FD-CT C-arm system.

Joachim Hornegger, Andreas K. Maier, André Aichert, Martin Berger and Michael Manhart are associated with the Pattern Recognition Lab, Friedrich-Alexander-Universität Erlangen-Nürnberg, Germany; Nicole Maass and Yu Deuerling-Zheng with the Siemens AG, Healthcare Sector, Erlangen and Forchheim, Germany; Arnd Doerfler and André Aichert with Department of Neuroradiology, Universitätsklinikum Erlangen, Germany; Andreas K. Maier with the Erlangen Graduate School in Advanced Optical Technologies (SAOT)

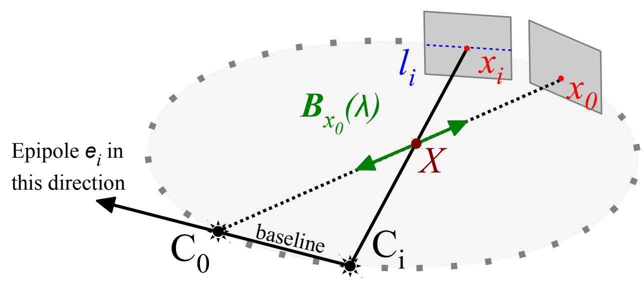

Figure 1. Epipolar geometry of two source positions $\mathbf{C}_0$ and $\mathbf{C}_i$ from a circular trajectory. An image point $\mathbf{x}_0 \cong \mathbf{P}_0\mathbf{X}$ on the detector is back-projected to a ray $\mathbf{B}_{\mathbf{x}_0}(\lambda)$. The line $\mathbf{l}_i \cong \mathbf{F}\mathbf{x}_i$ is the projection of that ray from $\mathbf{C}_i$ to the corresponding detector plane and hence contains the projection $\mathbf{x}_i \cong \mathbf{P}_i\mathbf{X}$ and the projection of the other source $\mathbf{e}_i \cong \mathbf{P}_i\mathbf{C}_0$, called the epipole. It follows that the line can be written as the join of the image point with the epipole $\mathbf{l}_i \cong \mathbf{e}_i \times \mathbf{x}_i$.

II. Epipolar Redundancies in X-ray Images

A. Epipolar Geometry

The term epipolar geometry describes the relative geometry between two pinhole cameras defined by their projection matrices $\mathbf{P}_0$ and $\mathbf{P}_i$. We rely on the real projective n-space $\mathbb{P}^n = \mathbb{R}^{n+1} \setminus \{\mathbf{0}\}$ and introduce an equality relation

$$\mathbf{a} \cong \mathbf{b} \Leftrightarrow \mathbf{a}, \mathbf{b} \in \mathbb{P}^n,\, \exists \lambda \in \mathbb{R},:\ \lambda\mathbf{a} - \mathbf{b} = \mathbf{0} \tag{1}$$

for the equivalence classes of scalar multiples. We will denote the location of the X-ray source as $\mathbf{C} \cong (-\mathbf{tR},\, 1)^T \cong kernel(\mathbf{P}) \in \mathbb{P}^3$, for the projection matrix $\mathbf{P} \cong \mathbf{K}[\mathbf{R}|\mathbf{t}] \in \mathbb{R}^{4\times3}$, according to the notation common in Computer Vision. The projection matrix $\mathbf{P}$ maps a world point in real projective three-space $\mathbf{X} \in \mathbb{P}^3$ to an image point on the detector in the real projective plane $\mathbf{x} \cong (u, v, 1)^T \cong \mathbf{PX} \in \mathbb{P}^2$. We will work with a large number of views, but consider only two pairs of projection matrices and images $(\mathbf{P}_0,\, I_0)$ and $(\mathbf{P}_i,\, I_i)$ at a time. For convenience, a lower index denotes the view number, for example, $\mathbf{x}_i \cong \mathbf{P}_i\mathbf{X}$ is a point in projective two-space on image I_i. W.l.o.g., we will use the index 0 as a reference view.

Suppose that the same world point is seen by two cameras as $\mathbf{x}_0 \cong \mathbf{P}_0\mathbf{X}$ and $\mathbf{x}_i \cong \mathbf{P}_i\mathbf{X}$. The intensity of a pixel $\mathbf{x}_0$ on the detector is the line integral along the back-projection ray $\mathbf{B}_{\mathbf{x}_0}(\lambda) \cong \mathbf{P}_0^{+}\mathbf{x}_0 + \lambda\mathbf{C}_0$, where $\cdot^{+}$ denotes the pseudo inverse. There exists a 3×3 matrix of rank 2 called the fundamental matrix $\mathbf{F}_0^i$ defined up to scale which maps a point $\mathbf{x}_0$ on the reference image I_0 to a line $\mathbf{l}_i \cong \mathbf{F}_0^i\mathbf{x}_0$ on I_i. The epipolar line $\mathbf{l}_i$ is the forward projection of a back-projection ray from a point on I_0 to I_i . Since the projection of $\mathbf{B}_{\mathbf{x}_0}$is the line $\mathbf{l}_i$ and $\mathbf{B}_{\mathbf{x}_0}$contains the source position $\mathbf{C}_0$, the line $\mathbf{l}_i$ must also contain the projection of $\mathbf{C}_0$ to the i-th image called the epipole $\mathbf{e}_i \cong \mathbf{P}_i\mathbf{C}_0$. Hence epipolar lines form a bundle around the epipole $\mathbf{l}_i \cong \mathbf{e}_i \times \mathbf{x}_i$. The fundamental matrix can be expressed directly in terms of the projection matrices

$$\mathbf{F}_0^i \cong [\mathbf{e}_i]_\times \mathbf{P}_i \mathbf{P}_0^{+} \tag{2}$$

where $[\mathbf{e}_i]_\times$ denotes the skew symmetric matrix representing the cross-product with the epipole. See also Figure 1 for an intuitive example and [1] for a thorough discussion.

B. 3D Radon Transform on Epipolar Planes

1) Notation: The key to finding redundancies imposed by this geometry is that the source positions $\mathbf{C}_0$, $\mathbf{C}_i$ and any back-projection ray $\mathbf{B}_{\mathbf{x}_0}$ define a plane, which contains both epipolar lines. There is a pencil of such planes around the line joining the source positions. We will now establish a relationship between the observed intensities along epipolar lines and the plane integral of the object over this epipolar plane. We call the plane $\mathbf{E} \cong join\,(\mathbf{B}_{\mathbf{x}_0}, \mathbf{C}_i) \cong (\mathbf{n}^T, -n)^T \in \mathbb{P}^3$ with normal $\mathbf{n}$ and signed distance from the origin n. W.l.o.g. assume that the origin of our coordinate system is in the (finite) X-ray source $\mathbf{C}_0$ with the z-axis pointing in orthogonal direction to an epipolar plane containing the back-projection ray $\mathbf{B}_{\mathbf{x}_0}$In this coordinate system the plane equation becomes $\mathbf{E} \cong (0,\,0,\,1,\,0)^T$, hence we need only consider x and y coordinates in the following. For points $\mathbf{x}_0^T\mathbf{l}_0 = \mathbf{b}$ on the epipolar line we introduce the notation $F_{\mathbf{x}_0}(r) := f(r \cdot cos(\varphi), r \cdot sin(\varphi), 0)$, where r is the distance to $\mathbf{C}_0 \cong (0,0,0,1)^T$ and φ is the ray direction within the plane $\mathbf{E}$ and $f : \mathbb{R}^3 \rightarrow \mathbb{R}$ denote the absorption coefficients of our object . $F_{\mathbf{x}_0}$ essentially samples f along the ray $\mathbf{B}_{\mathbf{x}_0}$.

2) 2D Radon Transform ρ_{I_0} along epipolar lines: We start from the X-ray intensity

$$I(u,v) = I_{\text{tube}} \cdot exp\left(-\int F_{\mathbf{x}_0}(r)\,dr\right) \tag{3}$$

detected in $\mathbf{x}_0 \cong (u,v,1)^T$ attenuated by an object f along the ray $\mathbf{B}_{\mathbf{x}_0}$with initial intensity I_{tube}. The X-ray projection for a single detector point on the 2D plane reads

$$ln\left(\frac{I_{tube}}{I(u,v)}\right) = \int F_{\mathbf{x}_0}(r)\,dr = \int f\begin{pmatrix} r \cdot cos(\varphi) \\ r \cdot sin(\varphi) \\ 0 \end{pmatrix} dr \tag{4}$$

where a single angleφ defines the ray, because by choice of coordinate system the source is in the origin. The distance to the origin r defines a point on that ray. Finally, the integral over an epipolar line $\mathbf{l}_0 \cong \mathbf{e}_0 \times \mathbf{x}_0$ in the polar coordinates of $\mathbf{E}$ is

$$\rho_{I_0}(\mathbf{l}_0) = \iint f\begin{pmatrix} r \cdot cos(\varphi) \\ r \cdot sin(\varphi) \\ 0 \end{pmatrix} drd\varphi \tag{5}$$

3) 3D Radon Transform ρ_f over the epipolar plane: The 3D radon transform of the object at $\mathbf{E}$ is the plane integral

$$\begin{aligned} \rho_f(\mathbf{E}) &= \iiint f(x,y,z)\delta((x,y,z,1)\cdot\mathbf{E})dxdydz \\ &= \iint f(x,y,0)dxdy \end{aligned} \tag{6}$$

If we write the same plane integral in terms of the polar coordinates, we get the relationship with the integral over the epipolar line $\mathbf{l}_0$. The Jacobian determinant of the polar transformation of the x-y-plane is exactly

$$det(\mathbf{J}_{\mathbf{\Phi}}) = r \cdot cos(\varphi)^2 + r \cdot sin(\varphi)^2 = r \tag{7}$$

which yields

$$\begin{aligned} \rho_f(\mathbf{E}) = \iint f(x,y,0)dxdy &= \iint f(\Phi(\varphi,r))det(\mathbf{J}_{\Phi})drd\varphi \\ = \iint f\begin{pmatrix} r \cdot cos(\varphi) \\ r \cdot sin(\varphi) \\ 0 \end{pmatrix} r\,drd\varphi &\neq \rho_{I_0}(\mathbf{l}_0) \end{aligned} \tag{8}$$

We observe for cone-beam projections, that the integrals over epipolar lines generally differ by a weighting with the distance to the X-ray source. In the following, we will derive a formulation of a derivative of the epipolar plane integral which happens to cancel out that weighting factor.

C. Grangeat's theorem

The relationship between line integrals on the projection image and plane integrals of the object has been investigated in a different context by Grangeat [3], [7]. For the moment, we restrict ourselves to a single projection image. If we assume w.l.o.g. that the origin of the u-v-plane is located in the principal point, we can write the epipolar line

$$\mathbf{l} \cong (cos(\psi + \frac{\pi}{2}),\, sin(\psi + \frac{\pi}{2}),\, -t)^T \tag{9}$$

in terms of an angle ψ and distance t from principal point $\mathbf{p}$. The point $\mathbf{o}$ is the orthogonal projection to that line. The 2D radon transform for $\mathbf{l}$ is

$$\rho_I(\mathbf{l}) = \iint I(u,v)\delta((u,v,1)\cdot\mathbf{l})\,dudv \tag{10}$$

Figure 2 (a) reveals the geometric relationships between the 2D radon transform $\rho_I(\mathbf{l})$ and the 3D radon transform of the object $\rho_f(\mathbf{E})$. The 3D distance from $\mathbf{C}$ to the line $\mathbf{l}$ is exactly the distance to the image plane within a projection in direction of t. Its orthogonal projection must therefore be again $\mathbf{o}$. It follows that the lines $join(\mathbf{p},\mathbf{o})$ and $join(\mathbf{C},\mathbf{o})$ are orthogonal to $\mathbf{l}$. An arbitrary point $\mathbf{x}$ on $\mathbf{l}$ can be written in terms of the angles κ (between $\mathbf{E}$ and the principal ray) and φ (between $\mathbf{o}$ and $\mathbf{x}$ measured at $\mathbf{C}$). The distance from $\mathbf{C}$ to $\mathbf{l}$ is then $cos(\varphi)r$ and the focal distance $cos(\kappa)cos(\varphi)\cdot r$ (via triangle $\mathbf{p}, \mathbf{C}, \mathbf{o}$).

Now, we apply Grangeat's trick and look at the derivative of $\rho(\mathbf{E})$ with respect to the distance to the origin n.

$$\frac{d}{dn}\rho_f(\mathbf{E}) = \frac{d}{dn}\iint F_{\mathbf{x}}(r)r\,drd\varphi = \iint \frac{d}{dn}F_{\mathbf{x}}(r)r\,drd\varphi \tag{11}$$

Observe in Figure 2 (b) that there is a relationship $dn = sin(d\kappa)\cdot cos(\varphi)r$. Because for small angles $sin(d\kappa) = d\kappa$ it holds

$$\frac{d\kappa}{dn} = \frac{1}{cos(\varphi)r} \tag{12}$$

and by chain rule we obtain

$$\frac{d}{dn}F_{\mathbf{x}}(r)r = \frac{d}{d\kappa}\frac{1}{cos(\varphi)}F_{\mathbf{x}}(r) \tag{13}$$

Since the angle φ is small (bounded by half fan-ange), the cosine is almost one and we ignore it in our computations. We also ignore that $\mathbf{n}$ is tilted slightly out of the detector plane, because κ is small. We can compute the derivative w.r.t t instead of n.

$$\begin{aligned}\frac{d}{dn}\rho_f(\mathbf{E}) &\overset{d\kappa\approx 0}{=} \iint \frac{d}{d\kappa}\frac{1}{cos(\varphi)}F_{\mathbf{x}}(r)\,drd\varphi \\ &\overset{\varphi \text{ small}}{\approx} \frac{d}{d\kappa}\iint F_{\mathbf{x}}(r)\,drd\varphi \overset{\kappa \text{ small}}{\approx} \frac{d}{dt}\rho_I(\mathbf{l})\end{aligned} \tag{14}$$

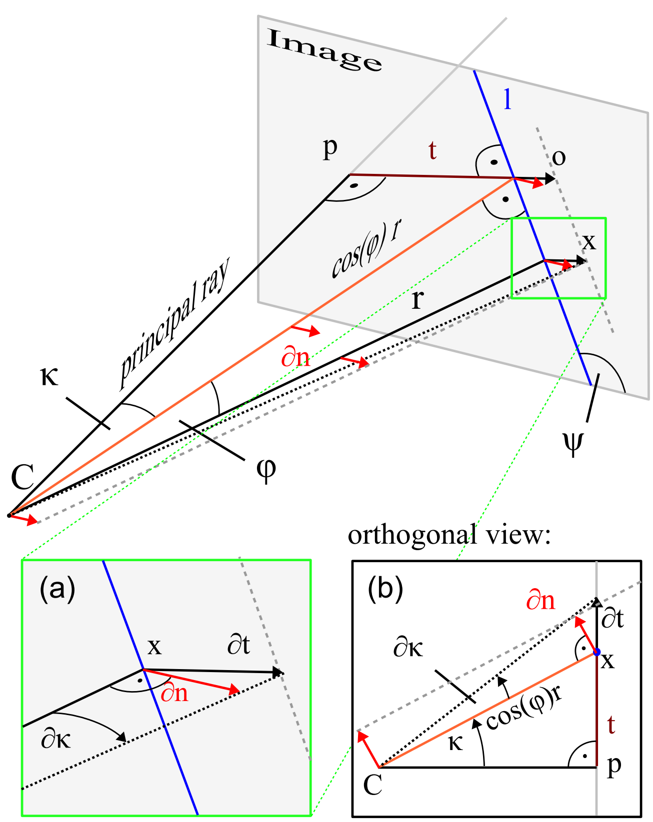

Figure 2. Grangeat's theorem: relationship between angle κ and normal n.

D. Definition of the metric

The main result of this paper and the connection between Equations 2 and 14 is that for a point $\mathbf{x}_0$ on I_0 we find redundant information in the i-th view (P_i, I_i)

$$M_0^i(\mathbf{x}_0) := \left(\frac{d}{dt}\rho_{I_0}(\mathbf{e}_0 \times \mathbf{x}_0) - \frac{d}{dt}\rho_{I_i}(\mathbf{F}_0^i\mathbf{x}_0)\right)^2 \approx 0 \tag{15}$$

The equation states, that given an image pair I_0 and I_i, a point $\mathbf{x}_0$ defines two corresponding epipolar lines $\mathbf{e}_0\times\mathbf{x}_0$ and $\mathbf{F}_0^i\mathbf{x}_0$, whose line integrals derived w.r.t t are approximately the same. This is assuming the projection is accurately known. We expect the line integrals to differ more or less, depending on the geometric accuracy of the epipolar plane, respectively the projection parameters.

As discussed in Section II-B1, there is a pencil of such epipolar planes and each defines a pair of redundant line integrals. Figure 3 shows the epipolar lines of two views along with their respective derivative of the radon transform. We define the epipolar consistency metric as the sum over the squared differences between a selection of corresponding epipolar lines. To exclude planes which do not intersect the projection images and to control the sampling, we select points $\mathcal{X}_0^i \subset \mathbb{P}^2$ on I_0, such that the resulting epipolar lines are evenly spaced, all intersect the images and that their maximal distance inside image bounds is no more than k pixels. We devise the following algorithm to select $\mathcal{X}_0^i$ for a finite epipole:

1) Find the most distant corner of I_0 to the epipole
$$\mathbf{e}_0^i \cong \mathbf{P}_0 \cdot \mathbf{C}_i \tag{16}$$
and call its distance m.
2) Compute the angular step $d\alpha$, such that
$$tan(d\alpha) = \frac{k}{m} \tag{17}$$
3) Find minimal and maximal angles α_{min}, α_{max}, so that any line
$$\mathbf{l}_\alpha = \left((cos(\alpha),\, sin(\alpha),\, 0)^T + e_0\right) \times \mathbf{e}_0 \tag{18}$$
intersects at least one image.
4) Compute the set $\mathcal{X}_0^i$ via
$$\begin{aligned}\mathcal{X}_0^i = \;\; &\{\mathbf{x}_0 \in \mathbb{P}^2 : \mathbf{x}_0 \cong (cos(\alpha),\, sin(\alpha),\, 0)^T + \mathbf{e}_0 \\ &\forall j \in \mathbb{N} : \alpha = \alpha_{min} + j\cdot d\alpha < \alpha_{max}\}\end{aligned} \tag{19}$$

In this formulation, the points in $\mathcal{X}_0^i$ lie on a circle around $\mathbf{e}_0$, no matter the radius. For (almost) infinite epipoles $\mathbf{e}_0 \cong (e_x, e_y, \epsilon)^T$, $\epsilon \approx 0$, one can simply assume it were finite and sufficiently far away. We can now express the metric as

$$M_0^i = \frac{1}{|\mathcal{X}_0^i|}\sum_{\mathbf{x}_0\in\mathcal{X}_0^i}\left(\frac{d}{dt}\rho_{I_0}(\mathbf{x}_0 \times \mathbf{e}_0) - \frac{d}{dt}\rho_{I_i}(\mathbf{F}_0^i\mathbf{x}_0)\right)^2 \tag{20}$$

divided by the number of line pairs $|\mathcal{X}_0^i|$. The derivatives of the 2D radon transform $\frac{d}{dt}\rho_I$ can be pre-computed.

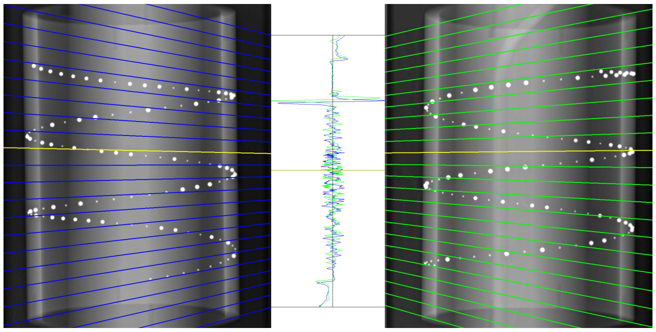

Figure 3. Two views with epipolar lines aligned to a plot of the derivative of the line integrals for the left image (blue) and right image (green). Notice a shift in the signals due to imperfect geometry.

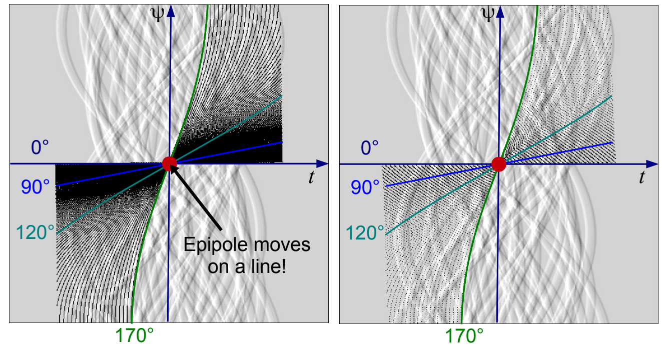

Figure 4. Derivative of the radon transform of the digital phantom. Samples for a 170° rotation about Y-axis with a maximum distance between epipolar lines of one pixel (left) and 5 pixels (right). Sampled locations in black.

Finally, we sum up all those pairs of views, which change during optimization. If we want to optimize over parameters in $\mathbf{P}_0$, for example, we need not compute redundancies between $(\mathbf{P_i}, I_i)$ and $(\mathbf{P}_j, I_j)$ for $i \neq 0 \neq j$, because they remain constant if only $\mathbf{P}_0$ changes: $M_0 = \sum_i M_0^i$.

III. Experiments and Results

A. Materials and methods

We validate against the digital phantom with random beads in a full 360° rotation presented in [4] (512×512 px projections, 1000 mm source-detector distance, phantom of diameter $\sim$ 100 mm). In addition, we conducted an experiment for this work using a 120° sweep of 190 projections showing a real PDS2 calibration phantom using a sequence of a Siemens C-arm system. Using [8] we computed the C-arm projection matrices from the projections of the metal beads in the calibration phantom and obtained an average re-projection error of about 1.3 pixels (image size 960×1240 px, bead size about $8 - 12$ px), which we also verified by visual inspection. These projection matrices are the gold standard. In order to prove the robustness of our method, we use the raw projection data directly from the scanner, without corrections of any kind (i.e. no I_0 correction, no correction for varying tube voltage etc.). We use a non-linear optimizer without gradient (Powell-Brent). In order to investigate accuracy, precision and stability of our method, we conduct a series of random studies over a rigid transformation in world space. As an intuitive and meaningful error metric, we compute the distance between the bead centers projected with the ground truth versus the current projection. This error is more informative, since the method itself is entirely image based, while quantities in millimeters and degrees of world space depend on overall scaling and most of the parameters a highly interdependent.

1) Sampling of radon space: In case of a circular trajectory, the epipole moves on a straight line from plus infinity, through the image to minus infinity. The epipolar lines are almost parallel, when the epipole is far away. When we align the detector v-axis with the axis of rotation, epipolar lines in most views will be almost parallel to the u-axis. This is visualized in Figure 4, where all the samples taken from radon space are marked with a black dot. Note that a line bundle corresponds to a sinoid curve in Radon Space. Also note a linear trajectory of the epipole leads to a single intersection point of all sinoids. This is because the epipole itself moves on a line, which is represented in a single point in radon space, and that line is contained in any of the line bundles. Through the definition of $\mathcal{X}_0^i$, we can easily adjust the number of lines, hence the sampling in radon space.

2) Dependency on direction of epipolar lines: We expect the method to be reliable whenever the epipole is close to the image or even inside the image. The epipole is inside the image when the two views are related dominantly by a forward-backward translation, including opposing views. For cases, where the epipolar lines are almost parallel, we get little information in their direction (the direction of the integrals) but only orthogonal to them. Note that a pure translation parallel to the image plane results in parallel epipolar lines, a translation orthogonal to the image plane leaves the epipole in the center of the image. Rotations around the source merely apply a 2D homography to the image. As a general motion is a combination of these effects, we can predict which geometries will give reliable information and in which spatial direction. Observe, for example Figure 4, where sampling is dense close to the $\psi = 0$ axis (horizontal). This is a property of any circular trajectory. The epipole is within the image for views within $\pm$ fan angle from the opposing view. For an opening angle of 40° this is just about 10 of all views. The method is thus much more robust for optimizing parameters orthogonal to the plane of rotation (usually denoted v-direction of the detector). Only for opposing views is it similarly reliable in both u and v directions. This is a problem especially for short scans, as visualized in the shape of the graphs in Figure 5, which show a long and narrow valley in u-direction.

B. Random study

1) Accuracy: First, the gold standard geometry is assumed and optimized w.r.t the metric to find the distance of the closest minimum. Any change away from the gold standard is an inaccuracy. We obtained a mean accuracy over all projections of ~ 0.25 px and a maximum of 1.00 px.

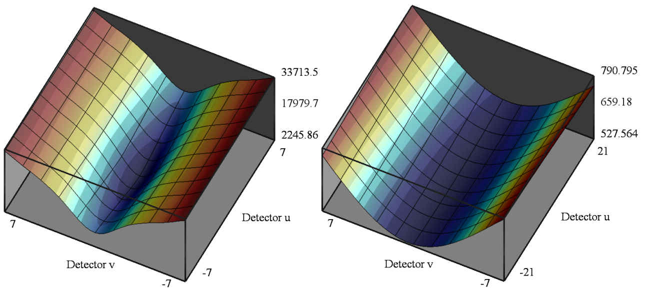

Figure 5. Plots of the epipolar consistency metric for detector shifts u and v for the numerical 360° phantom and the real 120° PDS2 phantom. Note the minimum can be located much more clearly in u-direction for 360° data.

2) Precision: The second step is to randomly disturb the optimal pose by a random set of parameters. The disturbances are uniformly distributed in a range of ± 5 mm for the translations and ± 0.05 radians $\approx \pm 2.8°$ for the rotations. We present results for only one representative projection at a sample size of $n = 30$. We were able to reduce the mean pixel error from ~ 2.4 px to ~ 0.2 px (maximum error was 0.7 px).

3) Stability: Finally, we conducted another random study with extreme disturbances of ± 25 mm for the translations and ± 0.25 radians $\approx \pm 14°$ for rotations and observe the range of parameters, for which optimization is successful. We found that of $n = 100$ samples drawn, with an average error of ~ 10 px we were able to recover the pose up to an error of < 1 px in 51 cases. The minimum initial error of the unsuccessful cases was 7.0 px and the mean initial error, which could be corrected for was 9.3 px.

4) Ultra short scan: Due to the direction of the epipolar lines for narrow angular range (compare Section III-A2), we conduct the random studies for the 120° data only w.r.t to the world Y-position of the source (similar to detector v) of the projection at 60° primary angle. This is currently a major limitation and subject of future work. The result of an initial random study for $n = 100$ and ± 25 mm offsets are a reduction of the mean error down from ~ 9.7 px to ~ 0.01 px with a maximum error of ~ 0.1 px. The same study for detector shift u would fail and even increase the mean error. This example shows, that a correct optimization strategy must be found.

IV. Conclusion

We present a new formulation for redundancies in transmission imaging data based on the epipolar geometry between pairs of views. We make the connection from Grangeat's theorem to the epipolar geometry of two X-ray projections, which enables us to express corresponding line integrals in the projection data using the fundamental matrix. We further derived a consistency metric, which exploits redundancies of these line integrals to optimize the projection geometry. We are presenting a fast algorithm to compute that metric and observe some of its properties, including robustness to varying X-ray tube parameters and its ability to correct 3D parameters, without the need for 3D reconstruction. The understanding of the underlying epipolar geometry gives us control over the sampling in radon space and it helps us identify geometries for which the metric is reliable. An initial random study using projections of a numerical and physical phantoms suggest that the metric can indeed find practical use in a multitude of applications related to the estimation of projection geometry. We believe that its potential applications range from pose estimation in fluoroscopy, tracking of a rigid object in X-ray projections, automatic re-calibration of the imaging system for FD-CT reconstruction up to the detection, estimation and correction of rigid patient movement. Future work should investigate different approches to optimization, such as finding subsets for reliable optmization, finding a minimal set of parameters to avoid dependencies in the optimization, evaluate real data sets and compare computation speed versus precision with other approches to calibration correction.

Acknowledgments: This work was supported by Spitzencluster Medical Valley, Verbund Bildgebende Diagnostik: Teilprojekt BD 16 FKZ: 13EX1212.

Disclaimer: The concepts and information presented in this paper are based on research and are not commercially available.

References

[1] R. I. Hartley and A. Zisserman, *Multiple View Geometry in Computer Vision*. Cambridge University Press, ISBN: 0521623049, 2000.

[2] O. Faugeras, *Three-dimensional computer vision: a geometric viewpoint*, ser. Artificial intelligence. MIT Press, 1993.

[3] P. Grangeat, "Mathematical framework of cone beam 3d reconstruction via the first derivative of the radon transform," in *Mathematical Methods in Tomography*, ser. Lecture Notes in Mathematics, G. Herman, A. Louis, and F. Natterer, Eds. Springer Berlin Heidelberg, 1991, vol. 1497, pp. 66–97.

[4] C. Debbeler, N. Maass, M. Elter, F. Dennerlein, and T. M. Buzug, "A new ct rawdata redundancy measure applied to automated misalignment correction," in *Proceedings of the Fully Three-Dimensional Image Reconstruction in Radiology and Nuclear Medicine (Fully3D)*, 2013, p. 264.

[5] W. Wein and A. Ladikos, "Detecting patient motion in projection space for cone-beam computed tomography," in *MICCAI 2011 Proceedings*, ser. Lecture Notes in Computer Science. Springer, Sep. 2011.

[6] Y. Kyriakou, R. M. Lapp, L. Hillebrand, D. Ertel, and W. A. Kalender, "Simultaneous misalignment correction for approximate circular cone-beam computed tomography," *Phys Med Biol*, vol. 53, no. 22, pp. 6267–6289, Nov 2008.

[7] T. Buzug, *Computed Tomography: From Photon Statistics to Modern Cone-Beam CT*. Springer, 2008.

[8] A. Maier, J. H. Choi, A. Keil, C. Niebler, M. Sarmiento, A. Fieselmann, G. Gold, S. Delp, and R. Fahrig, "Analysis of Vertical and Horizontal Circular C-Arm Trajectories," in *Proc. SPIE Vol. 7961*, SPIE, Ed., 2011, pp. 7 961 231–7 961 238.